Response to Reviewers

Date: 2026-11-02
Geoscientific Instrumentation Methods and Data Systems
Re: egusphere-2026-4378: Development of a UAV-based fully-airborne transient electromagnetic system, by Feng Guo et al.

Dear editor and reviewers,

Thank you for the opportunity to revise our manuscript entitled “Development of a UAV-based fully-airborne transient electromagnetic system” (Manuscript ID: egusphere-2026-4378). We greatly appreciate the time and effort that you have devoted to evaluating our work. The comments have been constructive and have helped us improve the quality, clarity, and rigor of the manuscript considerably.

In response to the reviewers’ comments, we have carried out additional analyses and revised the manuscript substantially. **All changes are highlighted in the revised manuscript using tracked changes, and page/line numbers cited below refer to the tracked version unless otherwise indicated.**

Below, we provide a point-by-point response to each comment. For clarity, the reviewers’ comments are shown in italics, followed by our response and a description of the changes made.

We hope that the revised manuscript is now suitable for further publication in Geoscientific Instrumentation Methods and Data Systems and look forward to hearing from you.

Sincerely, on behalf of all authors,

Ling Huang

Aerospace Information Research Institute, Chinese Academy of Sciences

huangling@aircas.ac.cn

Part I. Response to Reviewer 1

Comment 1.1

> *Comment 1.1: A number of key parameters of peer systems are missing in Table 1, which fails to intuitively demonstrate the comprehensive advantages of the proposed system. It is recommended to complete the key parameters of each system (including typical detection depth) to strengthen the comparative persuasiveness. A further comparison of the advantages and disadvantages of similar systems is also advised to highlight the merits of this work.*

Response: We have re-conducted a literature search on existing comparable systems. The results show that, apart from the Wukong system, for which an updated set of parameters has been publicly released, no other reliable source is currently available to fill the remaining gaps in the comparison table or to provide authoritative information on depth of investigation.

When discussing the advantages and limitations of existing systems, the proposed **three-component** UAV-based TEM system is, to our knowledge, the only one of its kind. Its advantage over conventional single-Z-component systems in rugged, sloped terrain is therefore intrinsic. Nevertheless, realizing this advantage in practice still relies on the accompanying data-processing and inversion workflow.

—**Lines [447]**:

However, former studies have proved that all-component interpretation takes more advantages in determining the range of anomalies and improving vertical and horizontal resolution (Chen et al., 2008). Yu et al. (2021) demonstrated that the 3-component TEM measurement has the potential of giving access to conductor information and the extension direction of anomalous body by numerical simulation.

Comment 1.2

> *Comment 1.2: Issues regarding technical details and writing standardization: The physical significance of variables in Equation (3) is not clearly stated, and supplementary explanations are needed. Grammatical errors exist in some sentences (e.g., "an easily equipment", "smaller work group is capable for deployment"), so professional English polishing of the entire manuscript is recommended.*

Response: We added the supplementary explanations following the Equation (3), which is Equation (6) currently due to a few newly added equations. Other grammatical errors have also been revised carefully to improve the expression.

—**Lines [429]**:

where $\vec{n}_{coil}$ denotes the instantaneous normal vector of the coil in the geographic (ENU) coordinate system. $R_{13}(t)$, $R_{23}(t)$, $R_{33}(t)$ are the elements in the of the time-varying rotation matrix $\boldsymbol{R}(t)$. $\vec{\mathrm{i}}$, $\vec{\mathrm{j}}$, $\vec{\mathrm{k}}$ are the unit vectors along the east, north and upward axes of the ENU geographic coordinate system, respectively.

—**Lines [7-519]** English polished for whole manuscript.

Comment 1.3

> *Comment 1.3: Electromagnetic interference (EMI) from UAV motors is one of the core challenges for airborne TEM systems. It is suggested to supplement the electromagnetic compatibility design of the proposed system and corresponding measured results, such as the amplitude and spectral distribution of motor EMI under different flight power conditions including hovering, level flight and speed variation.*

Response: Electromagnetic compatibility and UAV flight noise are indeed critical considerations for the system, which is also a concern raised by Reviewer 3. In response to the comments from both reviewers, we have added two sections, namely **3.1 Analysis of system dynamic noise** and **3.2 Design of electromagnetic compatibility.**

In section 3.1, we supplement experimental data acquired with the transmitter off and the towed bird flying at survey speed, and equivalent input magnetic-field(dB/dt) **dynamic noise** was quantified as a benchmark for further calculation.

In section 3.2, we introduced the EMI design and how the suspension length is decided.

—**Lines [328-373]**:

3.1 Analysis of system dynamic noise

The dynamic noise of an integrated airborne system is the noise level that the complete instrument reaches when it is carried by the aircraft and records data in flight. It therefore includes contributions that a bench test cannot reproduce, so the noise level is estimated from the scatter of the gate amplitudes between successive soundings rather than from the electronic noise of the receiver alone (Macnae et al., 1984);
Airborne TEM system uses the following expression to evaluate the dynamic noise level of the sounding system:

$$N_{d,j} = \sqrt{\frac{1}{N-1}\sum_{i=1}^{N}\left(d_{ij} - \bar{d}_j\right)^2}\,, \qquad (2)$$

where d_{ij} is the amplitude of gate j in the ith sounding, $\bar{d}_j$ its mean over the N soundings, and $N_{d,j}$ the noise of the gate, in nT/s.

The maximum designed sounding depth of the integrated UAV-borne system is 50 m. From the resistivity of a typical geological body, the latest TEM signal time that the system has to observe can be calculated as follows (Nabighian, 1979; Nabighian and Macnae, 1991):

$$\delta_{\mathrm{TD}} = \sqrt{\frac{2\rho t}{\mu_r \mu_0}}, \tag{3}$$

where δ_{TD} is the maximum sounding depth of the system, in m; t is the TEM propagation time, in s; ρ is the resistivity of the typical geological body, in Ω·m; μ_r is the relative permeability of the medium, dimensionless; and μ_0 is the permeability of free space, $4\pi\times10^{-7}$ H/m.

The test was carried out with the transmitter off and the towed bird flying at survey speed (2-4 m/s) more than 50 m above ground, continuous data were recorded at a sampling rate of 256 kHz and then decimated into time gates following standard TEM data processing procedures. Using the effective area of the sensor, the noise voltage at the receiver is converted to equivalent input magnetic field noise. The dynamic noise level of the late-time gate at 1 ms is calculated and compared with the acceptance threshold of 2 nT/s, a value below which indicates that the system has enough signal-to-noise ratio for the design exploration depth.

Figure 8 shows the equivalent input magnetic-field noise of the three receiving channels on logarithmic axes. At the 1 ms gate the equivalent input noise is 1.30 nT/s in Z, 1.70 nT/s in X and 0.82 nT/s in Y respectively. The integrated system therefore meets the design target of less than 2 nT/s in all three channels.

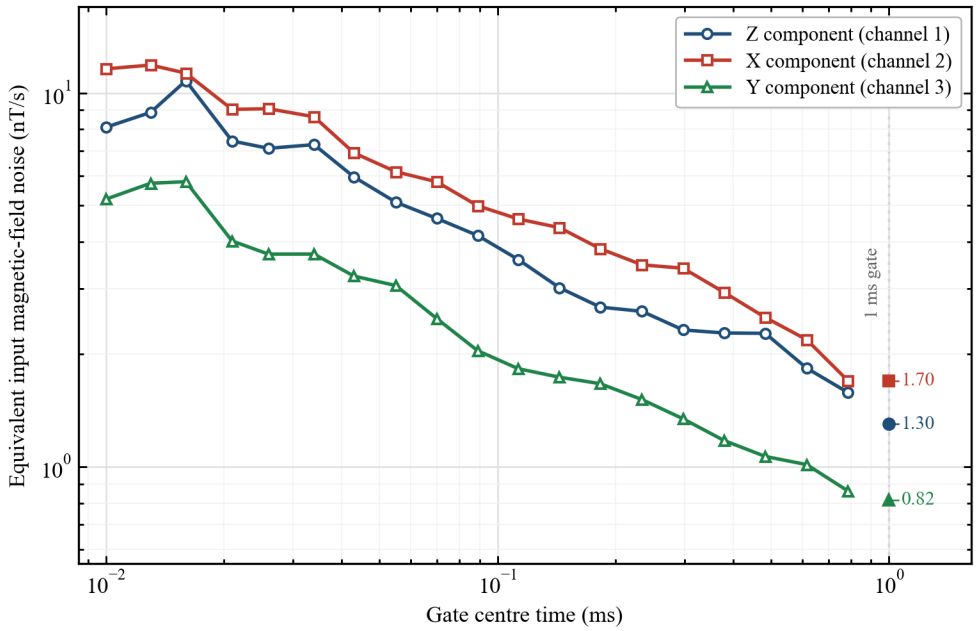


Figure 1 Equivalent input magnetic-field noise of the three receiver channels

3.2 Design of electromagnetic compatibility

Generally, there are two independent noise sources originated from the UAV platform: electromagnetic interference (EMI) radiated by the rotor motors and their drive electronics which coupled into the receiving coil through the near field, and motion noise arising from the swinging and rotation of the towed bird. A larger separation of suspension length attenuates the near-field magnetic coupling, which for a dipole-like source falls off as, whereas an excessive length degrades the stability of the towed bird and elevates the low-

frequency motion noise. The suspension length was therefore treated as a trade-off parameter to be fixed experimentally rather than simply maximized.

Comparative trials were carried out at site with low background noise, with the cable length set to 6, 10 and 12 m separately. The transmitter was switched off, and the coil was kept more than 50 m above ground throughout. With increasing suspension length, the narrow-band interference in the 70–95 kHz bands decreased markedly, and the spectrum above 1 kHz became smoother, indicating that a longer suspension suppresses the coupling of motor EMI into the coil. At 12 m, however, the bird oscillated visibly and pronounced baseline drift and low-frequency motion noise appeared in the raw data, degrading data quality.

However, noises originated from different UAV platforms differs in both frequency band and amplitude, and the proposed system is not designed for a particular flight platform. Therefore, in addition to electromagnetic compatibility, the safe distance for terrain-following flight and the safe operating clearance during take-off and landing are also important considerations, as some UAV platforms are restricted to a limited ground clearance by regulations.

Comment 1.4

> *Comment 1.4: It is recommended to add a quantitative analysis of the relationship among detection depth, formation resistivity and transmission parameters.*

Response: As suggested by reviewer, we added a new section **3.3 Analysis of detection depth** to discuss the theoretical detection depth under current system setting (transmission parameters, receiver dynamic noise)

—**Lines [374-403]**:

3.3 Analysis of detection depth

A two-layer geoelectric model was built to represent the typical electrical structure of a non-explicit landslide hazard. The resistivity of the upper layer was set to 20 Ω·m and that of the lower layer to 800 Ω·m. The depth of the interface between the two media was varied from 5 m to 50 m; for each interface depth, the responses of two models differing in interface depth by 1 m were computed and subtracted, so that the residual represents the signal produced by a 1 m offset of the interface.

The proposed system was assumed to fly at 5 m above the ground surface with a transmitting magnetic moment of 2250 A·m², which corresponds to the configuration of the proposed system.

The latest usable time gate that could be simulated is controlled mainly by the resistivity of the upper layer. In a homogeneous half-space, the transient field diffuses downwards as a smoke ring whose depth grows as $\sqrt{\rho t/\mu_0}$ (Nabighian, 1979; Raiche and Gallagher, 1985), and a buried interface becomes resolvable once the diffusion front has passed it, that is, at about one diffusion depth of overburden (Spies, 1989; Christiansen and Auken, 2012). The latest usable time gate is therefore estimated from

$$t = \frac{H^2}{784\rho\cdot},$$

(4)

where t is the delay after turn-off (ms), H is the maximum detection depth (m) and ρ is the apparent resistivity (Ω·m). Equation (4) is not the analytical smoke-ring solution, but a practical engineering approximation for estimating the latest interpretable late-time gate. In this study, it is used only to select the evaluation time gate for noise assessment, rather than for rigorous depth of investigation inversion. For a two-layer medium the target is the interface itself, so the background apparent resistivity reduces to the resistivity of the upper layer.

For an upper-layer resistivity of 10 Ω·m, equation (4) gives the latest simulation time of 0.3 ms. The analysis of slip surfaces and groundwater levels shallower than 50 m is therefore restricted to delays shorter than 0.3 ms. Within this window the response difference produced by a 1 m offset of the interface was compared with the dynamic noise level of the system, a difference being regarded as detectable only when it exceeds that level.

The maximum difference was extracted along the depth axis between 10 m and 80 m, and the response differences against interface depth are illustrated in Fig. 9. The grey dashed horizontal line marks the dynamic noise level of the system, taken conservatively as 2 nT/s.

Between 5 and 50 m the difference produced by a 1 m offset of the interface remains above 2 nT/s, therefore exceeds the dynamic noise level of the developed system at every interface depth considered. A response difference induced by 1 m displacement of the slip surface is thus theoretically observable by the proposed system within the 50 m depth range of interest.

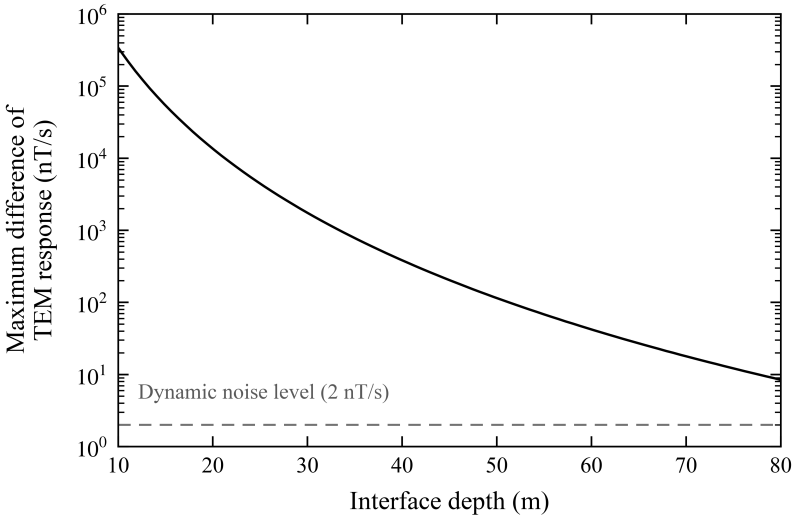


Figure 2 Airborne TEM response difference versus depth

Comment 1.5

Comment 1.5: The paper mentions that the transmitter turn-off dead time degrades the detectability of extremely shallow targets, but provides no specific value of the dead time

> *or the corresponding depth of the detection blind zone. It is suggested to quantify this technical limitation.*

Response: In the revised manuscript, we incorporate the measured turn-off dead time of the system. Based on the detection depth, applicable scenarios were given, and alternative solutions for near surface exploration were discussed.

—**Lines [189-210]**:

Transmitter function and performance tests, as well as synchronous transmit/receive decoding tests were conducted. And Fig. 3 illustrates the test results of the actual transmitted pulse, verifying that the system can generate alternating high- and low-current dual pulses. The transmit current exhibits excellent stability within the flat-top interval and across successive pulse cycles. Under 24V power supply conditions, the dual-clamping constant voltage up to 500V could be reached, and the clamping voltage level remains stable during current shutdown, ensuring the linearity of shutdown current. Transmission capability experiments with an equivalent load proved that the transmitted current could reach 20A±0.3A, with a turn-off time of 12μs@20A.

—**Lines [512-575]**:

Despite the aforementioned advantages, UAV-based fully airborne TEM systems still suffer from transmitter turn-off dead time, which may reduce their detectability of extremely shallow targets. Furthermore, constraints on UAV payload capacity, power consumption, and flight time limit the overall system scale, thereby restricting the achievable transmitting magnetic moment and the excitation capability for deep targets. Therefore, in practical field surveys, multi-depth joint exploration integrating complementary geophysical methods is required. UAV-borne magnetic surveys and ground-penetrating radar can be employed to compensate for the limitations in ultra-shallow detection.

Part II. Response to Reviewer 2

Comment 2.1

> *Comment 2.1: The abstract presents complete research logic and sufficient quantitative technical parameters, but the research novelty and technical improvements over conventional airborne TEM systems are not explicitly highlighted. In particular, the comparison with current technics.*

Response: We have revised the abstract as suggested and highlighted the innovations and the distinctions from conventional airborne TEM systems, while making the abstract more insightful.

—**Lines [7-17]**:

In response to the challenges of transient electromagnetic (TEM) exploration in complex terrain, a lightweight, low-noise, three-component, fully-airborne TEM system based on an unmanned aerial vehicle (UAV) platform is designed, offering improved terrain adaptability and survey efficiency compared with existing semi-airborne UAV-based TEM systems. Three-component electromagnetic field measurement enables reliable detection of the normal component, even over undulating terrain, and provides a theoretical basis for correcting errors caused by receiver coil oscillation. Through system-level optimization, the proposed system achieves a balance between weight and transmission power, featuring a lightweight configuration(14.94 kg), a large transmitting magnetic moment (2250 Am^2), and an extremely low system dynamic noise level (1.7 nT/s). A series of performance verification experiments and field tests verify the stability and practical operability of the proposed system under field application. Furthermore, comparisons between the inversion results obtained from the acquired survey data and borehole logging data provide additional evidence of the system's reliability. Therefore, this system offers an effective technical approach and solid data support for the fine detection of subsurface interfaces at depths of up to 50 m.

Comment 2.2

> *Comment 2.2: Section 2.1 uses a lot long compound sentences, which could be difficult to follow for readers. A simplified description is necessary.*

Response: We have carefully revised Section 2.1: cumbersome long compound sentences are split, and the descriptions are simplified and restructured.

—**Lines [185-249]**:

2.1 Design and development of low-power high-magnetic-moment TEM transmitter

This research on high-frequency pulse fast turn-off technology was conducted to achieve TEM transmission with rapid current turn-off, high transmitter magnetic moment, low power consumption, and compact form factor. The dual-clamping topology applies high-voltage clamping to both the positive and negative edges of the transmit current, enabling linear, fast edge ramps and supporting the generation and precise regulation of high-quality electromagnetic pulse waveforms. As shown in Fig. 2, through a segmented control design that divides the positive edge into a clamping stage and an exponential stage, the electromagnetic response excited by the positive edge of the high-frequency pulse does not interfere with that induced by the negative-edge turn-off excitation.The power switching and power inverter circuits transmit dual pulses, with both large and small magnetic moments to achieve blind zone suppression and high-precision detection in both deep and shallow areas. While increasing the peak transmission current, the TEM pulse width is further compressed to reduce the power consumption.

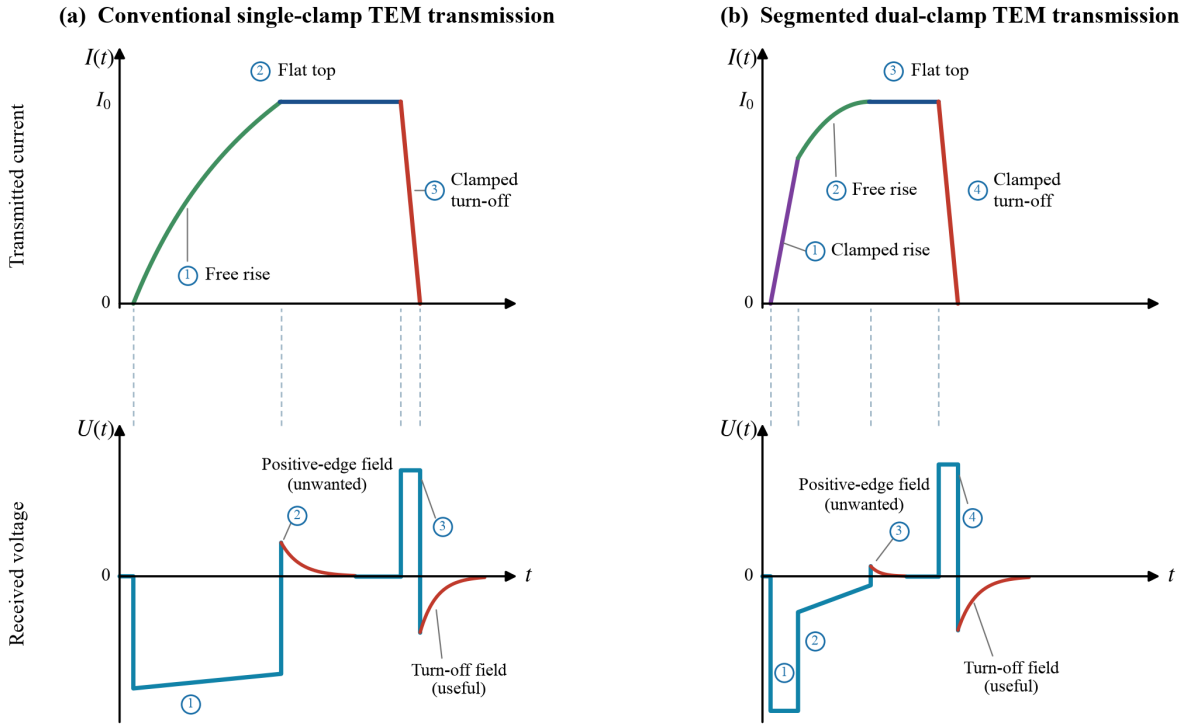


Figure 3 Timing diagram for segmented dual-clamping transmitters

The proposed TEM transmitter adopts a high-speed power switching architecture for power inversion, rapid supply commutation, and segmented adjustable active constant-voltage dual clamping. Three galvanically isolated internal power supplies are deployed to mitigate electrical crosstalk and improve control stability.. The power components adopted a high-speed MOSFET full-bridge inverter circuit to achieve rapid shut-down and improve detection resolution.

Transmitter function and performance tests, as well as synchronous transmit/receive decoding tests were conducted. And Fig. 3 illustrates the test results of the actual transmitted pulse, verifying that the system can generate alternating high- and low-current dual pulses. The transmit current exhibits excellent stability within the flat-top interval and across successive pulse cycles. Under 24V power supply conditions, the dual-clamping constant voltage up to 500V could be reached, and the clamping voltage level remains stable during

current shutdown, ensuring the linearity of shutdown current. Transmission capability experiments with an equivalent load proved that the transmitted current could reach 20A±0.3A, with a turn-off time of 12μs@20A.

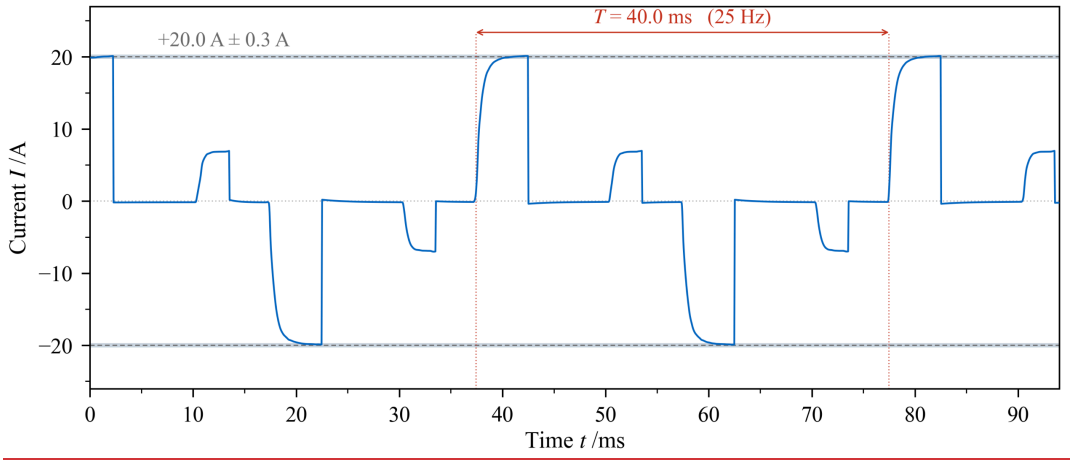


Figure 4 Test result of transmitted pulse current

Comment 2.3

> *Comment 2.3: Line.105: The design of high-precision synchronous clock is used to provide time matching between transmitter and receiver, and it could also be noticed from Fig.1 that there is a synchronization cable between transmitter and receiver, therefore what is that used for?*

Response: We designed two synchronization schemes for the transmitter and receiver systems. The first relies on a synchronization cable, while the second is cable-free and achieves clock synchronization by referencing a common reference clock (GPS pulse per second, PPS). Therefore, we have added explanations in the manuscript.

—Lines [277-279]:

The receiver also integrates a high-precision synchronous clock calibration circuit to provide the system with highly stabled local synchronous clock signal for time matching between the transmitter and receiver. Alternatively, time synchronization can be achieved via a synchronization cable connection.

Comment 2.4

> *Comment 2.4: How is the lightweight towed bird design realized in section 2.4? Is it achieved by lightweight materials, structural optimization, or other measures?*

Response: We explained the implementation of system lightweighting in Section 2.4, which is mainly realized via innovative structural design and the adoption of lightweight materials.

—**Lines [340-341]**:

To achieve lightweight design of towed-bird, carbon fibre material is used to form the transmitting loop supporting former. A novel scheme with integrated loop structure is devised to lower the aerodynamic drag and mass of the transmitting coil.

Comment 2.5

> *Comment 2.5: Are the inversion results presented in Fig. 10 derived from threecomponent data?*

Response: This inversion uses only three-component data for motion noise suppression.

—**Lines [ ]**:

Part III. Response to Reviewer 3

Comment 3.1

> *Comment 3.1: Line 26: remove "developed by Hydro Geophysics". There is no such company.*

Response: Revised as suggested.

—**Lines [26]**:

The SkyTEM system is one of the most sophisticated helicopter-borne transient electromagnetic (HTEM) platform as well.

Comment 3.2

> *Comment 3.2: Line 30: fields --> field*

Response: Revised as suggested.

—**Lines [31]**:

The emergence of UAVs has revolutionized this field by providing a lower-altitude, terrain-following alternative.

Comment 3.3

> *Comment 3.3: Line 40: filed --> field*

Response: Revised as suggested.

—**Lines [135]**:

Nevertheless, the system still weighs 150kg, requiring a heavy lift drone for field operations (Nyboe et al., 2024).

Comment 3.4

> *Comment 3.4: Line 65: Please explain the dual clamping in more detail. It might be beneficial to add a figure with a block diagram or timing diagram.*

Response: The detailed explanation of dual clamping has been added to the manuscript as well as a timing diagram as suggested.

—Lines [185]:

This research on high-frequency pulse fast turn-off technology was conducted to achieve TEM transmission with rapid current turn-off, high transmitter magnetic moment, low power consumption, and compact form factor. The dual-clamping topology applies high-voltage clamping to both the positive and negative edges of the transmit current, enabling linear, fast edge ramps and supporting the generation and precise regulation of high-quality electromagnetic pulse waveforms. As shown in Fig. 2, through a segmented control design that divides the positive edge into a clamping stage and an exponential stage, the electromagnetic response excited by the positive edge of the high-frequency pulse does not interfere with that induced by the negative-edge turn-off excitation.The power switching and power inverter circuits transmit dual pulses, with both large and small magnetic moments to achieve blind zone suppression and high-precision detection in both deep and shallow areas. While increasing the peak transmission current, the TEM pulse width is further compressed to reduce the power consumption.

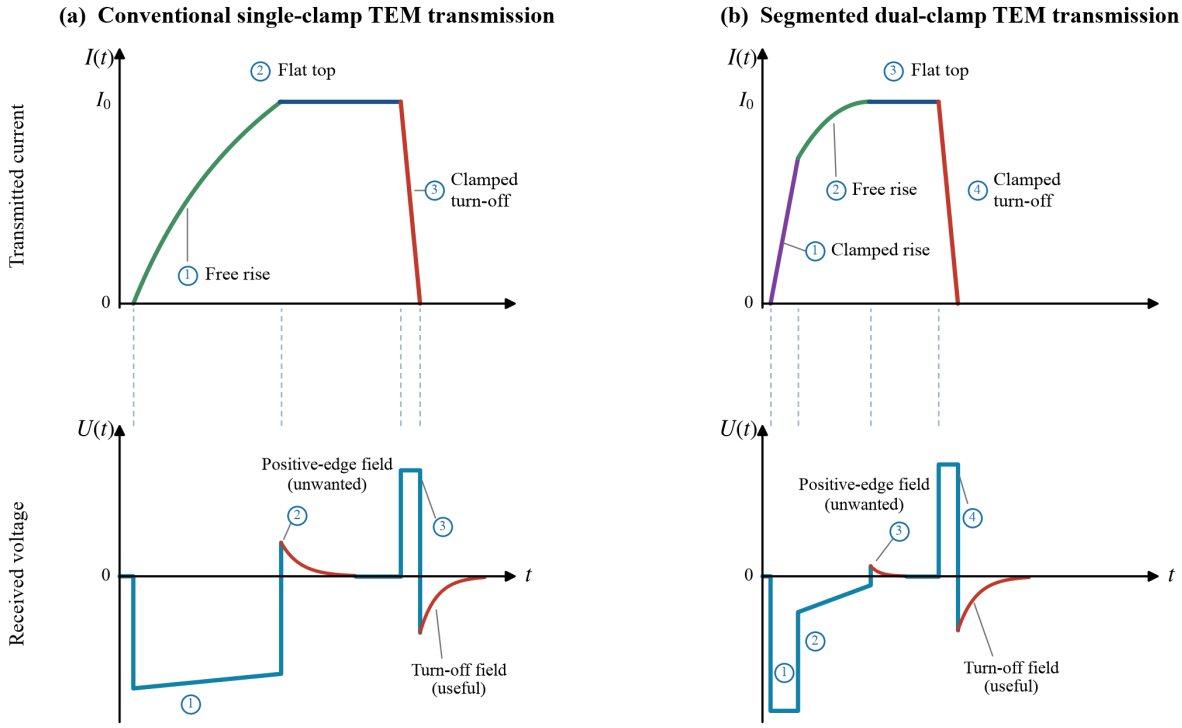


Figure 5 Timing diagram for segmented dual-clamping transmitters

Comment 3.5

> *Comment 3.5: Line 79: The stability of the transmitter cannot be judged from figure 2. It would be appropriate with some statistical measures, e.g., the peak current is 20.0±0.5 A or similar.*

Response: Revised as suggested.

—**Lines [231]**:

Transmission capability experiments with an equivalent load proved that the transmitted current could reach 20A±0.3A, with a turn off time of 12μs@20A.

Comment 3.6

> *Comment 3.6: Figure 2: This appears to be a screenshot from a digital oscilloscope. It is somewhat pixelated and the time axis cannot be seen directly but must be inferred. I suggest that the author load the data into, e.g., MATLAB, and make a proper figure.*

Response: Revised as suggested.

—**Lines [234]**:

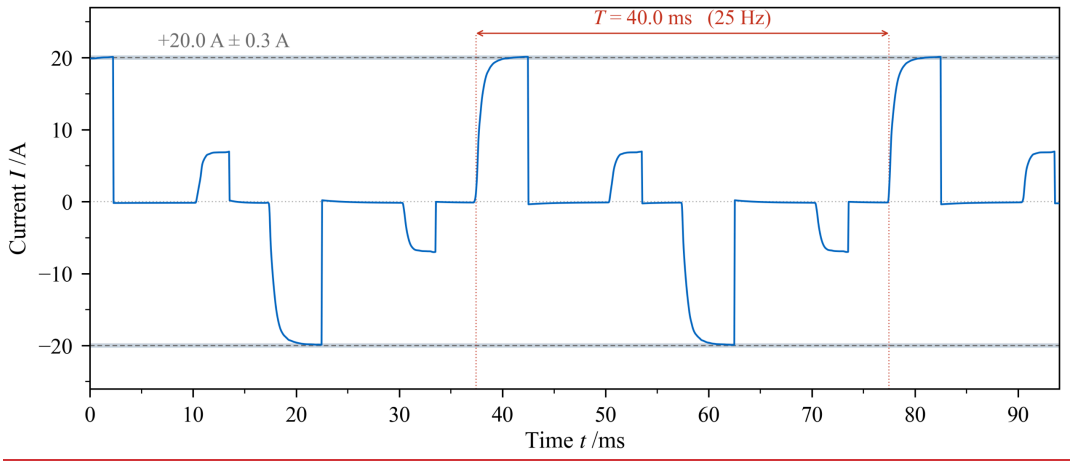


Figure 6 Test result of transmitted pulse current

Comment 3.7

> *Comment 3.7: Line 86: Is "Research" really the right word here. From the manuscript content "development" seems more appropriate.*

Response: Revised as suggested.

—Lines [250]:

2.2 Development of multi-channel signal acquisition technology

Comment 3.8

> *Comment 3.8: Line 87: The authors are not very clear on the actual sensor. Does it measure magnetic field or does it measure the derivative of the magnetic field by measuring the voltage across an induction coil?*

Response: We appreciate the reviewer for pointing out the unclear definitions in the manuscript. This sensor measures the derivative of the magnetic field (dB/dt) by measuring the voltage across an induction coil, and we have added the corresponding descriptions in the revised manuscript

—**Lines [310]**:

The designed sensor directly measures the time derivative of the magnetic field dB/dt, rather than the magnetic field B.

Comment 3.9

> *Comment 3.9: Line 88-89: I don't see any circuit design in Figure 3.*

Response: We revised our expression to match the content of Fig.3 (Fig.4 now).

—**Lines [252]**:

The internal structure design is illustrated in Fig. 4, where OCXO denotes an oven-controlled crystal oscillator, PL the programmable logic, and PS the processing system. The latter two being the two sections of the Zynq system-on-chip.

Comment 3.10

> *Comment 3.10: Figure 3: Not all readers will easily understand all the abbreviations. Please explain PL, PS, OCXO in the caption or in the text. What is the meaning of "1" in Hx1?*

Response: We added explanations of above-mentioned abbreviations for a better understand in the manuscript. As for the meaning of "1" in Hx1, we revised the expression in Fig. 4 to make a better understanding, and here C_x, C_y, C_z represent Channel X, Channel Y, Channel Z.

—Lines [252]:

The internal structure design is illustrated in Fig. 4, where OCXO denotes an oven-controlled crystal oscillator, PL the programmable logic, and PS the processing system. The latter two being the two sections of the Zynq system-on-chip.

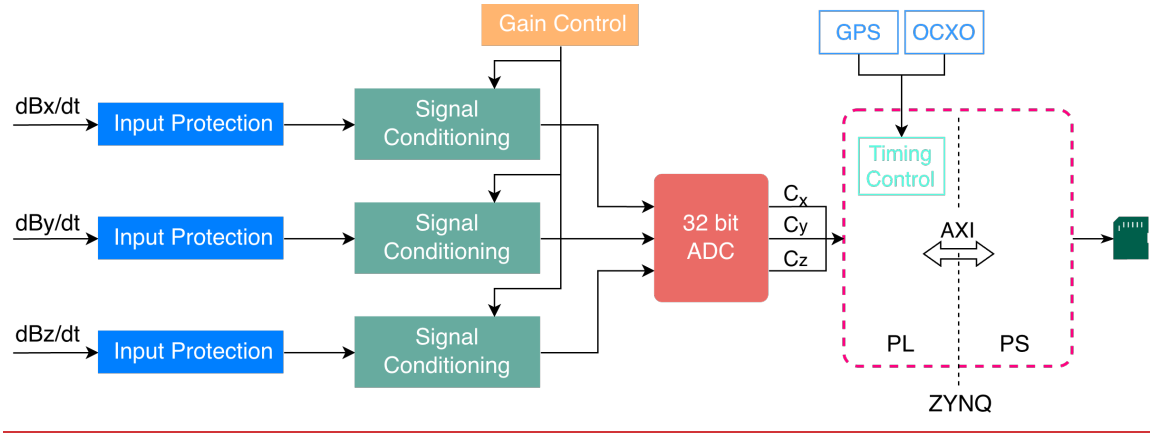


Figure 7 Block diagram of developed signal receiver

Comment 3.11

> *Comment 3.11: Line 103: Date --> Data*

Response: Revised as suggested.

—Lines [276]:

The ARM processor then caches the data in double data rate (DDR) memory.

Comment 3.12

> *Comment 3.12: Line 106: It is not obvious how "the noise level of the receiver" was tested. Is it possible that it is only the noise level of a short-circuited amplifier that is tested? Please add details.*

Response: This suggestion is indeed very helpful for improving the quality of our manuscript. In our original text, we only mentioned "dynamic noise" without providing its definition and measurement method. **This noise is actually measured during dynamic flight with the transmitter turned off**. Following the reviewer's further comments, we have reorganized this part and presented it in detail as a standalone **Section 3.1 Analysis of system dynamic noise,** which we believe is more meaningful.

—**Lines [368-396]**:

3.1 Analysis of system dynamic noise

The dynamic noise of an integrated airborne system is the noise level that the complete instrument reaches when it is carried by the aircraft and records data in flight. It therefore includes contributions that a bench test cannot reproduce, so the noise level is estimated from the scatter of the gate amplitudes between successive soundings rather than from the electronic noise of the receiver alone (Macnae et al., 1984);

Airborne TEM system uses the following expression to evaluate the dynamic noise level of the sounding system:

$$N_{d,j} = \sqrt{\frac{1}{N-1}\sum_{i=1}^{N}\left(d_{ij} - \bar{d}_j\right)^2}\,, \tag{2}$$

where d_{ij} is the amplitude of gate j in the ith sounding, $\bar{d}_j$ its mean over the N soundings, and $N_{d,j}$ the noise of the gate, in nT/s.

The maximum designed sounding depth of the integrated UAV-borne system is 50 m. From the resistivity of a typical geological body, the latest TEM signal time that the system has to observe can be calculated as follows (Nabighian, 1979; Nabighian and Macnae, 1991):

$$\delta_{\mathrm{TD}} = \sqrt{\frac{2\rho t}{\mu_r \mu_0}}\,, \tag{3}$$

where δ_{TD} is the maximum sounding depth of the system, in m; t is the TEM propagation time, in s; ρ is the resistivity of the typical geological body, in Ω·m; μ_r is the relative permeability of the medium, dimensionless; and μ_0 is the permeability of free space, $4\pi\times10^{-7}$ H/m.

The test was carried out with the transmitter off and the towed bird flying at survey speed (2-4 m/s) more than 50 m above ground, continuous data were recorded at a sampling rate of 256 kHz and then decimated into time gates following standard TEM data processing procedures. Using the effective area of the sensor, the noise voltage at the receiver is converted to equivalent input magnetic field noise. The dynamic noise level of the late-time gate at 1 ms is calculated and compared with the acceptance threshold of 2 nT/s, a value below which indicates that the system has enough signal-to-noise ratio for the design exploration depth.

Figure 8 shows the equivalent input magnetic-field noise of the three receiving channels on logarithmic axes. At the 1 ms gate the equivalent input noise is 1.30 nT/s in Z, 1.70 nT/s in X and 0.82 nT/s in Y respectively. The integrated system therefore meets the design target of less than 2 nT/s in all three channels.

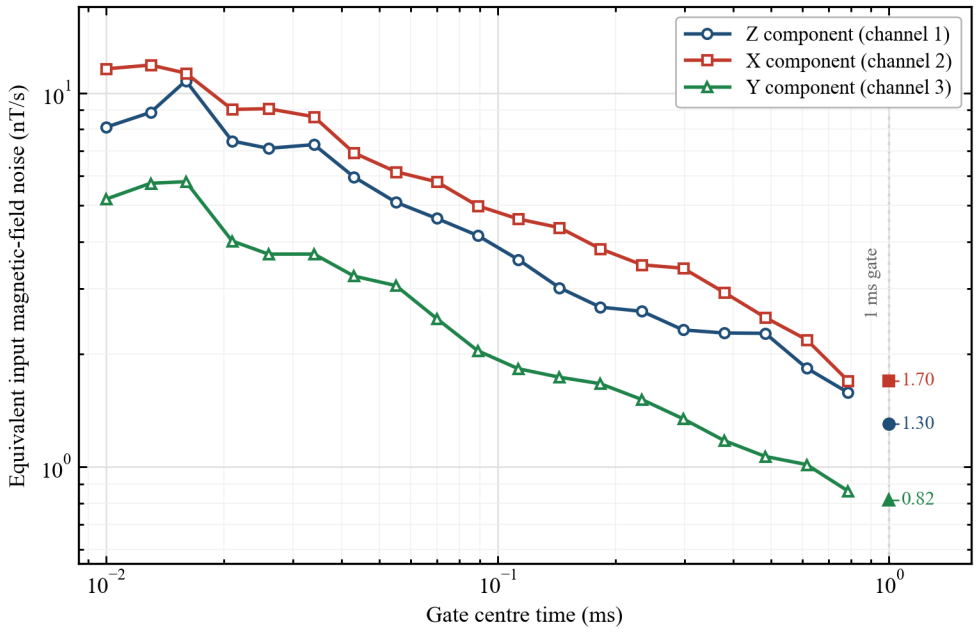


Figure 8 Equivalent input magnetic-field noise of the three receiver channels

Comment 3.13

> *Comment 3.13: Line 107: Why is the noise level for X and Z quoted with three significant digits while only two are used for Y?*

Response: We have revised the description as suggested at first. However, when writing Section 3.1, the dynamic noise level was converted to the magnetic field. Accordingly, while fully considering this comment, we removed the original content and replaced it with more informative and referential data.

—**Lines [389]**:

Figure 8 shows the equivalent input magnetic-field noise of the three receiving channels on logarithmic axes. At the 1 ms gate the equivalent input noise is 1.30 nT/s in Z, 1.70 nT/s in X and 0.82 nT/s in Y respectively. The integrated system therefore meets the design target of less than 2 nT/s in all three channels.

Comment 3.14

> *Comment 3.14: Figure 4: This figure should be revised. It is bad practice to use unequal scaling across the three figures. I suggest that the three data sets are plotted on one graph instead. This will make similarities and differences among channels immediately appear.*

Response: This Figure is now replaced by a newly plotted Figure 8 for equivalent input magnetic-field noise of the three receiver channels. As suggested, the three-channel data are presented together within this single figure.

—**Lines [395]**:

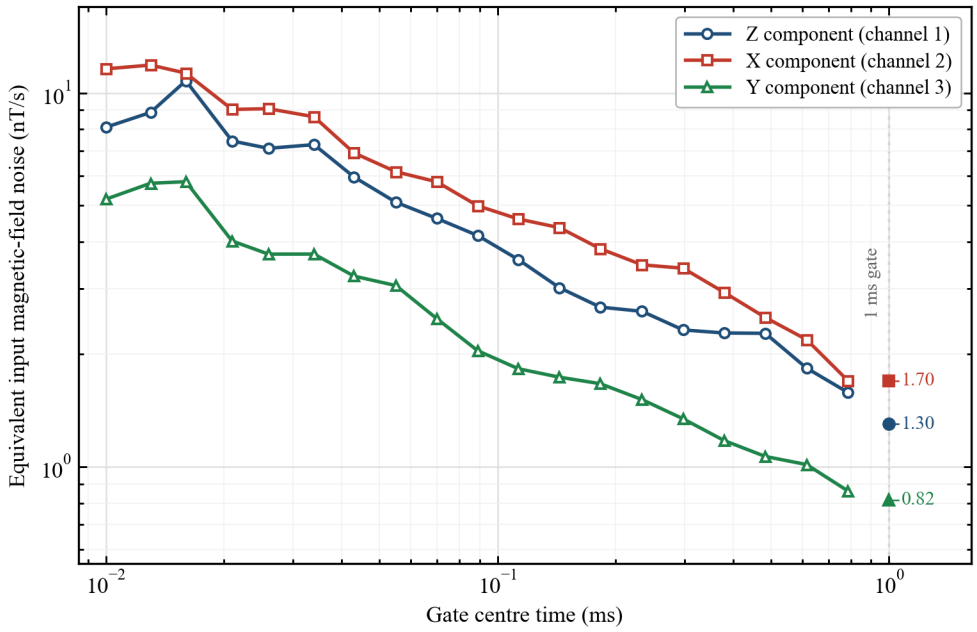


Figure 9 Equivalent input magnetic-field noise of the three receiver channels

Comment 3.15

> *Comment 3.15: Line 120: It is not clear to me what definition of bandwidth is used here. If nothing else is quoted I would assume a 3 dB bandwidth. However, the signal drops by two orders of magnitude across the plot in figure 5B. Please revise.*

Response: This misunderstanding arose because we did not provide a clear definition of the sensor type in the original manuscript, and we have corrected this issue as suggested. We provided detailed explanation of the sensor type and the meaning of HNOM in the Fig.5B, since the sensor is working in a differentiating mode, the -3 dB bandwidth criterion is not adopted in this work.

—**Lines [310]**:

The designed sensor directly measures the time derivative of the magnetic field dB/dt, rather than the magnetic field B. The HNOM (nominal magnetic field transfer coefficient) shown in Fig. 6(b) characterizes this transfer relationship, whose magnitude increases linearly with frequency and presents an inherent high-pass response. As Tumański (2007) summarized, the differentiating coil has no flat passband to serve as a reference gain level, so the -3 dB bandwidth criterion is not adopted in this work（Metwally, 2013）.

Comment 3.16

> *Comment 3.16: Line 124: The authors mention a compensation coil, but it is not discussed. I assume the compensation coil is just what is normally referred to as a bucking coil. Please add details on this issue.*

Response: The compensation coil here is just what is normally referred to as a bucking coil. We added details of this compensation coil as suggested.

—**Lines [329]**:

The transmitting coil adopts a primary-field compensation technique at the centre to suppress the electromagnetic response of conventional TEM systems arising from the turn-off time and the mutual inductance effect between the transmitting and receiving coils. This approach compensates the strong primary field component in the received signals, achieves weak coupling between the transmitting and receiving coils.

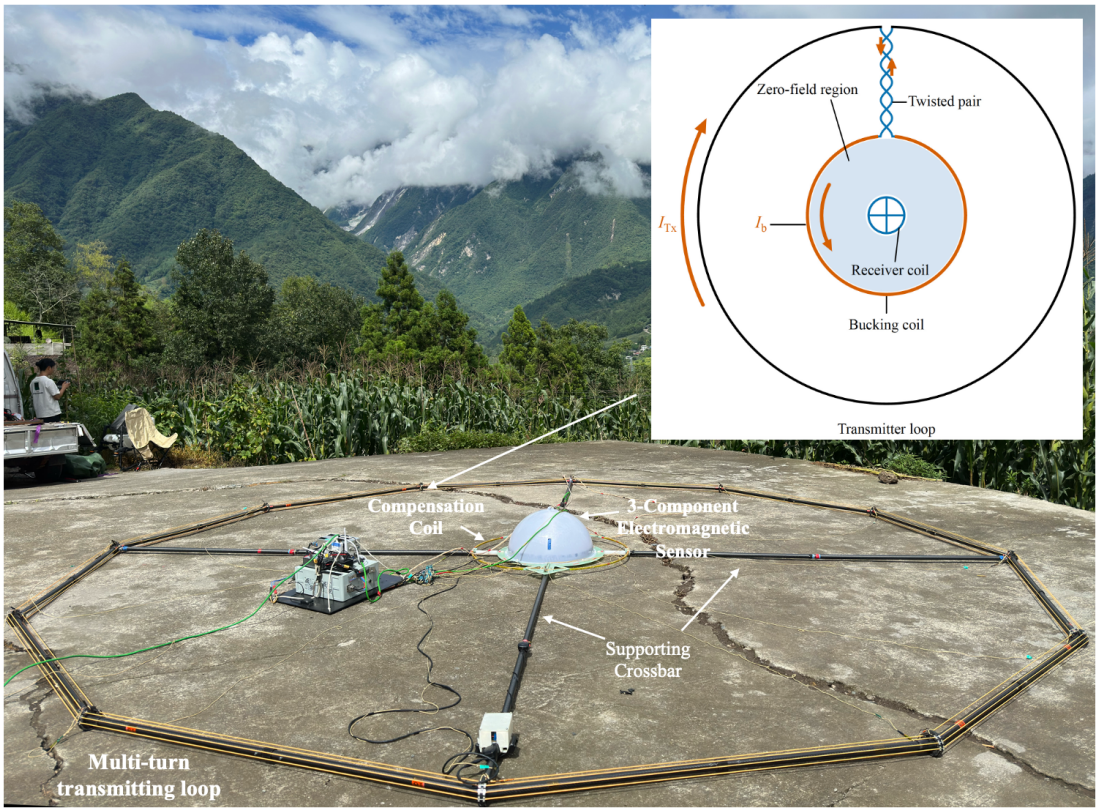


Figure 10 Design of lightweight TEM towed-bird

Comment 3.17

> *Comment 3.17: Line 145: An important feature of a UAV system is the actual flight time, but this number is missing in the manuscript.*

Response: We added the actual operation time in the manuscript as suggested. However, this flight duration was measured based on the DJI-T100 platform and is not representative of performance for other UAV platforms.

—Lines [516]:

(7) Flight time: 15-20min (based on DJI T100).

Comment 3.18

> *Comment 3.18: Figure 7: The figure shows a 10 m distance between drone and payload. How was this distance decided. What is the level of noise in the data caused by interference from the drone?*

Response: UAV flight noise and Electromagnetic compatibility (10m suspension length) are indeed critical considerations for the system, which is also a concern raised by Reviewer 1. In response to the comments from both reviewers, we have added two sections, namely **3.1 Analysis of system dynamic noise** and **3.2 Design of electromagnetic compatibility.**

In section 3.1, we supplement experimental data acquired with the transmitter off and the towed bird flying at survey speed, and equivalent input magnetic-field(dB/dt) **dynamic noise** was quantified as a benchmark for further calculation.

In section 3.2, we introduced the EMI design and explained how the suspension length is decided.

—**Lines [328-373]**:

3.1 Analysis of system dynamic noise

The dynamic noise of an integrated airborne system is the noise level that the complete instrument reaches when it is carried by the aircraft and records data in flight. It therefore includes contributions that a bench test cannot reproduce, so the noise level is estimated from the scatter of the gate amplitudes between successive soundings rather than from the electronic noise of the receiver alone (Macnae et al., 1984);

Airborne TEM system uses the following expression to evaluate the dynamic noise level of the sounding system:

$$N_{d,j} = \sqrt{\frac{1}{N-1}\sum_{i=1}^{N}\left(d_{ij} - \bar{d}_j\right)^2}\,, \tag{2}$$

where d_{ij} is the amplitude of gate j in the ith sounding, $\bar{d}_j$ its mean over the N soundings, and $N_{d,j}$ the noise of the gate, in nT/s.

The maximum designed sounding depth of the integrated UAV-borne system is 50 m. From the resistivity of a typical geological body, the latest TEM signal time that the system has to observe can be calculated as follows (Nabighian, 1979; Nabighian and Macnae, 1991):

$$\delta_{\mathrm{TD}} = \sqrt{\frac{2\rho t}{\mu_r \mu_0}}\,, \tag{3}$$

where δ_{TD} is the maximum sounding depth of the system, in m; t is the TEM propagation time, in s; ρ is the resistivity of the typical geological body, in Ω·m; μ_r is the relative permeability of the medium, dimensionless; and μ_0 is the permeability of free space, $4\pi\times10^{-7}$ H/m.

The test was carried out with the transmitter off and the towed bird flying at survey speed (2-4 m/s) more than 50 m above ground, continuous data were recorded at a sampling rate of 256 kHz and then decimated into time gates following standard TEM data processing procedures. Using the effective area of the sensor, the noise voltage at the receiver is converted to equivalent input magnetic field noise. The dynamic noise level of the late-time gate at 1 ms is calculated and compared with the acceptance threshold of 2 nT/s, a value below which indicates that the system has enough signal-to-noise ratio for the design exploration depth.

Figure 8 shows the equivalent input magnetic-field noise of the three receiving channels on logarithmic axes. At the 1 ms gate the equivalent input noise is 1.30 nT/s in Z, 1.70 nT/s in X and 0.82 nT/s in Y respectively. The integrated system therefore meets the design target of less than 2 nT/s in all three channels.

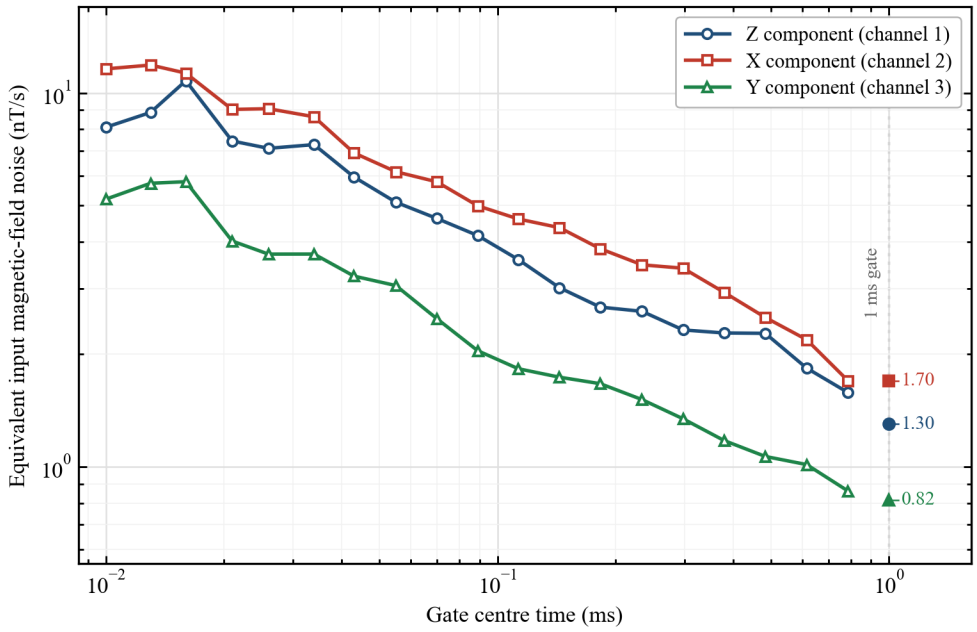


Figure 11 Equivalent input magnetic-field noise of the three receiver channels

3.2 Design of electromagnetic compatibility

Generally, there are two independent noise sources originated from the UAV platform: electromagnetic interference (EMI) radiated by the rotor motors and their drive electronics which coupled into the receiving coil through the near field, and motion noise arising from the swinging and rotation of the towed bird. A larger separation of suspension length attenuates the near-field magnetic coupling, which for a dipole-like source falls off as, whereas an excessive length degrades the stability of the towed bird and elevates the low-frequency motion noise. The suspension length was therefore treated as a trade-off parameter to be fixed experimentally rather than simply maximized.

Comparative trials were carried out at site with low background noise, with the cable length set to 6, 10 and 12 m separately. The transmitter was switched off, and the coil was kept more than 50 m above ground throughout. With increasing suspension length, the narrow-band interference in the 70–95 kHz bands decreased markedly, and the spectrum above 1 kHz became smoother, indicating that a longer suspension suppresses the coupling of motor EMI into the coil. At 12 m, however, the bird oscillated visibly and pronounced baseline drift and low-frequency motion noise appeared in the raw data, degrading data quality.

However, noises originated from different UAV platforms differs in both frequency band and amplitude, and the proposed system is not designed for a particular flight platform. Therefore, in addition to electromagnetic compatibility, the safe distance for terrain-following flight and the safe operating clearance during take-off and landing are also important considerations, as some UAV platforms are restricted to a limited ground clearance by regulations.

Comment 3.19

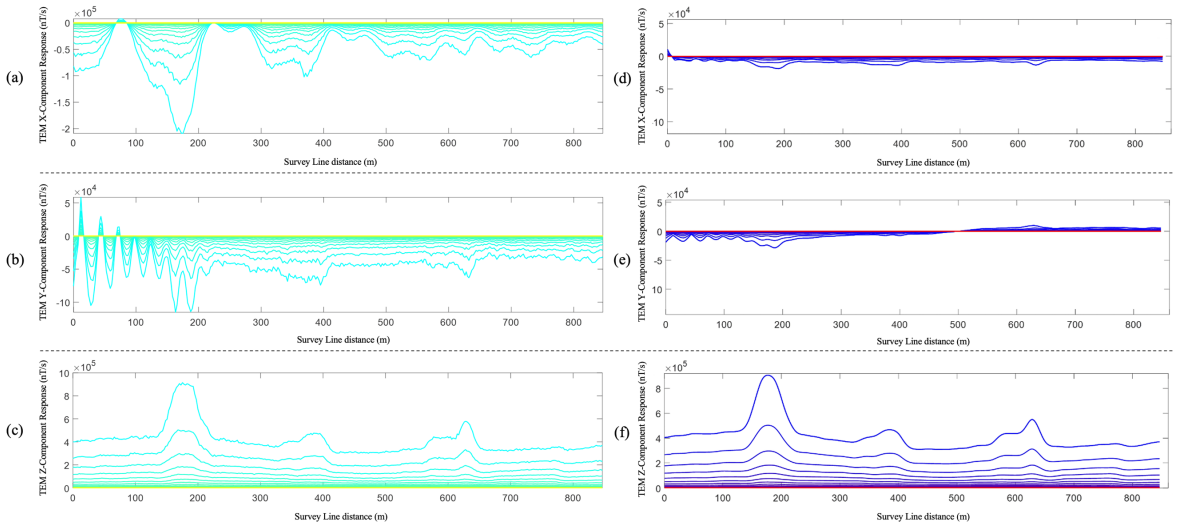
> *Comment 3.19: Figure 8: I suggest that the figure is augmented with a couple of standard sounding examples, i.e. a log-log plot of dB/dt signal versus time following a single pulse. This would make it easier for the reader to assess the data quality.*

Response: We sincerely thank the reviewer for this valuable suggestion. We fully agree that such a quantitative comparison would be very effective in demonstrating the performance of the correction algorithm to the readers.

However, the main purpose of the present section is to illustrate how the proposed approach corrects the TEM response caused by coil oscillation during field operation, and to highlight the advantage of three-component TEM data acquisition in this regard. From this perspective, we believe that the existing figure already conveys the influence of attitude correction on the measured TEM response and is sufficiently informative for the readers to assess the correction effect.

Nevertheless, we have taken the reviewer's comment into serious consideration. We have reorganized Fig. 12 into a 2×3 layout, with the the three components arranged in columns. Horizontal dashed lines separate the three component rows to facilitate side-by-side comparison of the uncorrected (left) and corrected (right) responses.

—**Lines [504]**:

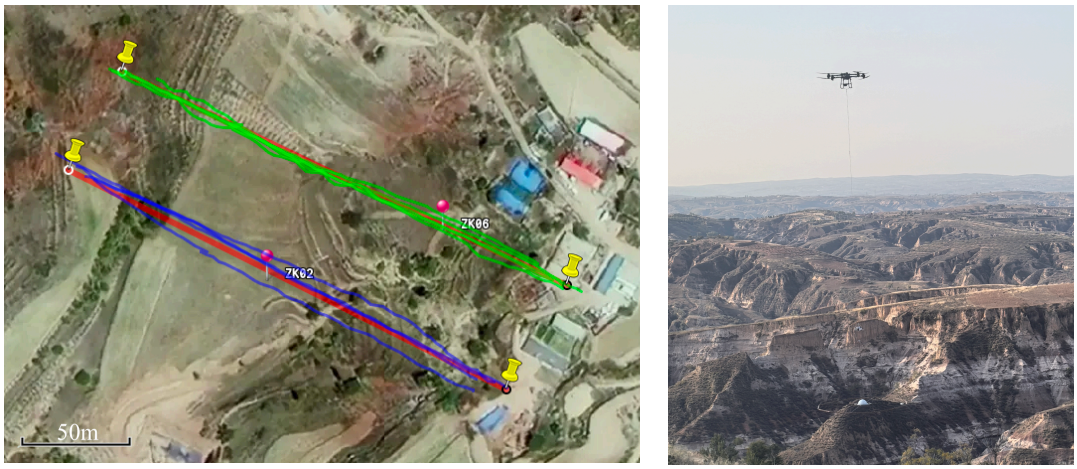


Comment 3.20

> *Comment 3.20: Figure 9: Please indicate the size of the survey on the map by adding a ruler. What is the cause of the somewhat large deviations from the intended flight path?*

Response: We have added a ruler as suggested on the map to indicate the size of the survey. As for the offsets between survey lines, they arose during terrain-following flights over deeply incised terrain, where the UAV pilot operated the aircraft fully manually, especially under high wind speeds. Repeated flights were conducted in this experiment to guarantee the validity of the measurements.

—**Lines [519]**:



(a) (b)

Figure 12 Proposed system in application. (a) Planned survey line and actual flight trajectory; (b) Picture of system in exploration`

Comment 3.21

> *Comment 3.21: Line 200, Table 2: Data are here quoted with a precision of 1 cm. This number is clearly completely out of context given, e.g., the footprint of the EM field at 30 m depth. If you insist on this precision, please explain how it comes about.*

Response: We established a resistivity–lithology interface to delineate the actual landslide surface. Therefore, the depth result presented in this study was derived from this lithology-based interface (i.e., the dashed line in Fig. 12), and its accuracy does not rely solely on conventional electrical-resistivity inversion, as we explained in the manuscript:

—**Lines [528]**: However, to obtain an accurate stratigraphic interface, the relationship between resistivity and lithology was constructed (Ruffet et al., 1995; Jin et al., 2024; Auken et al., 2017), resulting in the predicted landslide surface boundary shown by the dashed line in Fig. 12(a) & (b).

Comment 3.22

> *Comment 3.22: Line 221, Discussion. An important problem in airborne measurements is motion-induced noise, which can be significant for TEM, where movements of the receiver coil in the earth magnetic field can give dB/dt variations much larger than the TEM signal. However, this issue is not discussed in the manuscript. It would be appropriate to add this. A figure with flight data from a measurement done without turning on the transmitter could provide insight.*

Response: We added a new section namely **3.1 Analysis of of system dynamic noise** and provide a figure of noise level from a measurement done without turning on the transmitter at a survey speed.

—**Lines [368-396]**:

3.1 Analysis of system dynamic noise

The dynamic noise of an integrated airborne system is the noise level that the complete instrument reaches when it is carried by the aircraft and records data in flight. It therefore includes contributions that a bench test cannot reproduce, so the noise level is estimated from the scatter of the gate amplitudes between successive soundings rather than from the electronic noise of the receiver alone (Macnae et al., 1984);

Airborne TEM system uses the following expression to evaluate the dynamic noise level of the sounding system:

$$N_{d,j} = \sqrt{\frac{1}{N-1}\sum_{i=1}^{N}\left(d_{ij} - \bar{d}_j\right)^2}\,, \quad (2)$$

where d_{ij} is the amplitude of gate j in the ith sounding, $\bar{d}_j$ its mean over the N soundings, and $N_{d,j}$ the noise of the gate, in nT/s.

The maximum designed sounding depth of the integrated UAV-borne system is 50 m. From the resistivity of a typical geological body, the latest TEM signal time that the system has to observe can be calculated as follows (Nabighian, 1979; Nabighian and Macnae, 1991):

$$\delta_{\mathrm{TD}} = \sqrt{\frac{2\rho t}{\mu_r \mu_0}}, \quad (3)$$

where δ_{TD} is the maximum sounding depth of the system, in m; t is the TEM propagation time, in s; ρ is the resistivity of the typical geological body, in Ω·m; μ_r is the relative permeability of the medium, dimensionless; and μ_0 is the permeability of free space, $4\pi\times10^{-7}$ H/m.

The test was carried out with the transmitter off and the towed bird flying at survey speed (2-4 m/s) more than 50 m above ground, continuous data were recorded at a sampling rate of 256 kHz and then decimated into time gates following standard TEM data processing procedures. Using the effective area of the sensor, the noise voltage at the receiver is converted to equivalent input magnetic field noise. The dynamic noise level of the late-time gate at 1 ms is calculated and compared with the acceptance threshold of 2 nT/s, a value below which indicates that the system has enough signal-to-noise ratio for the design exploration depth.

Figure 8 shows the equivalent input magnetic-field noise of the three receiving channels on logarithmic axes. At the 1 ms gate the equivalent input noise is 1.30 nT/s in Z, 1.70 nT/s in X and 0.82 nT/s in Y respectively. The integrated system therefore meets the design target of less than 2 nT/s in all three channels.

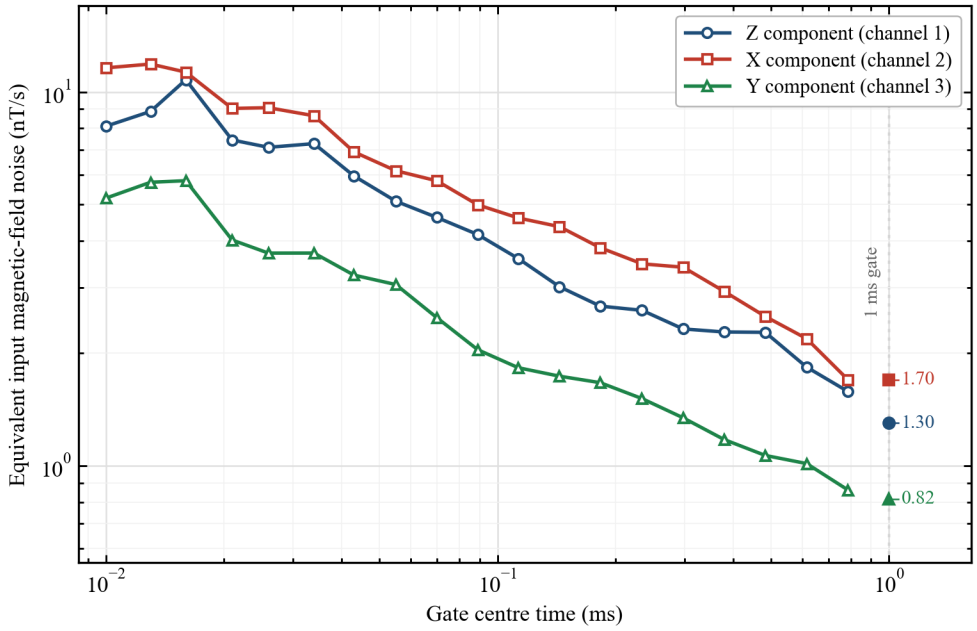


Figure 13 Equivalent input magnetic-field noise of the three receiver channels

Comment 3.23

> *Comment 3.23: Line 221, Discussion. This section is not particularly insightful. Line 225-232 belongs in the introduction to the manuscript and line 236-243 is a conclusion, not a discussion.*

Response: We have revised the Discussion as suggested to a Conclusion.

—**Lines [538-615]**:

5 Conclusion

The successful development of the proposed system represents a breakthrough in lightweight, high-efficiency, UAV-based fully airborne TEM detection technology. Based on the field application results and interpreted data, the reliability of the proposed system has been demonstrated.

Compared with similar technologies, the existing UAV-based TEM detection mainly uses a semi-airborne configuration, which has a ground stationary transmitter and a drone-towed receiver. The proposed system developed a “air-transmitted and air-received” operation mode, representing a significant advancement in both exploration efficiency and terrain adaptability.

To achieve the above-mentioned results, the following innovations have been implemented: 1) An innovative segmented dual-clamping high-current transmission scheme was adopted to achieve narrow-pulse, high-magnetic-moment signal transmission while significantly reducing average power consumption. This fundamentally addresses the heavy payload and high power-consumption associated with traditional helicopter-borne systems. 2) A high-performance three-component electromagnetic field sensor was developed, significantly improving the sensitivity and signal-to-noise ratio of data acquisition. 3) A lightweight, transceiver-integrated towed bird was designed to improve the system's suitability for complex field application scenarios, thereby significantly enhancing exploration stability and reliability.

Despite the aforementioned advantages, UAV-based fully airborne TEM systems still suffer from transmitter turn-off dead time, which may reduce their detectability of extremely shallow targets. Furthermore, constraints on UAV payload capacity, power consumption, and flight time limit the overall system scale, thereby restricting the achievable transmitting magnetic moment and the excitation capability for deep targets. Therefore, in practical field surveys, multi-depth joint exploration integrating complementary geophysical methods is required. UAV-borne magnetic surveys and ground-penetrating radar can be employed to compensate for the limitations in ultra-shallow detection.

Comment 3.24

> *Comment 3.24: Line 234. The use of “pioneered” is overselling. E.g., the authors refer in Table 1 to three existing systems.*

Response: We have revised our expression as suggested.

—**Lines [543]**:

The proposed system developed a “air-transmitted and air-received” operation mode, representing a significant advancement in both exploration efficiency and terrain adaptability.